NANO LETTERS

pubs.acs.org/NanoLett Letter

Manipulating Moirés by Controlling Heterostrain in van der Waals Devices

Ian Sequeira,[†] Andrew Z. Barabas,[†] Aaron H Barajas-Aguilar, Michaela G Bacani, Naoto Nakatsuji, Mikito Koshino, Takashi Taniguichi, Kenji Watanabe, and Javier D. Sanchez-Yamagishi*

Cite This: *Nano Lett.* 2024, 24, 15662−15667 Read Online

ACCESS | Metrics & More | Article Recommendations | Supporting Information

ABSTRACT: Van der Waals (vdW) moirés offer tunable superlattices that can strongly manipulate electronic properties. We demonstrate the *in situ* manipulation of moiré superlattices via heterostrain control in a vdW device. By straining a graphene layer relative to its hexagonal boron nitride substrate, we modify the shape and size of the moiré. Our sliding-based technique achieves uniaxial heterostrain values exceeding 1%, resulting in distorted moirés values that are larger than those achievable without strain. The stretched moiré is evident in transport measurements, resulting in shifted superlattice resistance peaks and Landau fans, consistent with an enlarged superlattice unit cell. Electronic structure calculations reveal how heterostrain shrinks and distorts the moiré Brillouin zone, resulting in a reduced electronic bandwidth as well as the appearance of highly anisotropic and quasi-one-dimensional Fermi surfaces. Our heterostrain control approach opens a wide parameter space of moiré lattices to explore beyond what is possible by twist angle control alone.

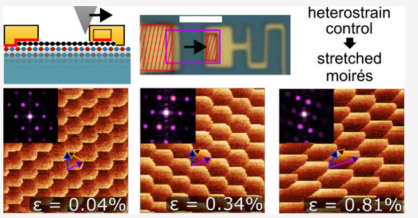

KEYWORDS: *van der Waals materials, moirés, heterostrain, graphene, hexagonal boron nitride, electronic transport*

Moiré materials offer highly tunable superlattices with length scales that are unattainable in natural crystals. The extreme sensitivity of the electronic behaviors and correlated states to the moiré structure motivates the precise control of moiré patterns, especially *in situ* manipulation techniques.[1−4] These efforts have primarily focused on controlling the relative twist angle, which determines the size of the moiré pattern but cannot alter its shape or symmetry.

Strain control offers an alternative route to manipulating moiré patterns beyond what is possible via twist angle, where both the size and symmetry of the moiré can be altered. To strongly distort the moiré, it is necessary to strain adjacent layers by different amounts, which is referred to as heterostrain. The possibility of achieving large heterostrain is a unique feature of van der Waals (vdW) materials due to exceptionally low interlayer shear strengths.[5] When two lattices form a moiré, the effects of heterostrain are amplified by a moiré factor $\sim 1/(\delta - \varepsilon)$, where δ is the mismatch between the lattices and ε is the strain in one layer. This factor diverges as ε approaches δ and has a directionality set by the strain direction. As a result, heterostrain can strongly distort the moiré, changing its size and symmetries in a way not possible when straining both layers simultaneously (Figure 1a−c).[6,7] Correspondingly, heterostrain can also strongly manipulate moiré systems' electronic structure, especially in flatband systems such as twisted bilayer graphene.[7−10]

To date, the experimental study of heterostrain has been limited by the challenge of controllably producing a uniform and large heterostrain. Local probes such as scanning tunneling microscopy or optical measurements have been successful in

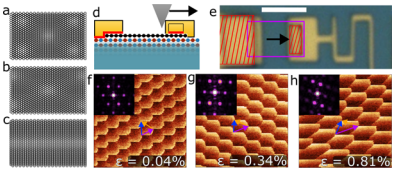

Figure 1. Controlling heterostrain to manipulate vdW moirés formed between graphene and hBN. (a−c) Cartoon hexagonal lattices with a δ = 10% lattice mismatch: (a) unstrained, (b) 2% uniaxial heterostrain, (c) 10% uniaxial heterostrain. (d) Side view schematic of a stretchable open-face g-hBN device. The graphene is stretched by pushing one electrode with an AFM tip (gray triangle). Red lines indicate areas where the metal is strongly adhered via the O_2-plasma treatment before deposition. (e) Optical image of device B. Red dashed regions are O_2-plasma treated. Purple box outlines the graphene channel. Scale bar is 4 μm. (f−h) 100 nm × 100 nm CAFM images of g-hBN moirés in device A. The CAFM x-axis is orientated along the channel, parallel to the attempted stretching direction. Inset shows FFT of the image. Fitting the wavevectors results in the indicated strain values ε ($\pm$3e−4 uncertainty) with strain angles relative to the +x-axis of +80 ± 20°, +1 ± 5°, +17 ± 4° and twist angles −0.12°, 0.02°, 0.02° for parts f, g, h, respectively. All parameters and uncertainties are listed in Supporting Information Table 1.

Received: August 29, 2024
Revised: November 15, 2024
Accepted: November 19, 2024
Published: November 25, 2024

https://doi.org/10.1021/acs.nanolett.4c04201
Nano Lett. 2024, 24, 15662−15667

measuring the effects of heterostrain on spectroscopic features,[11−17] but transport measurements have been more limited due to the need for uniform heterostrain over larger areas. Current transport studies have relied on moiré heterostrain introduced accidentally in the nanofabrication process.[8,18] Such strain profiles are generally small and of uncontrolled direction and homogeneity. Progress has been made in controlling strain in vdW heterostructure devices by stretching or bending the underlying substrate[19−21] or by using deposited stressors.[22−24] For all approaches, an outstanding challenge is to achieve large and controlled heterostrain in a high-quality moiré device.

Here, we demonstrate the control of uniaxial heterostrain in graphene-hexagonal boron nitride (g-hBN) devices and study its effects on moiré structure and transport properties. To achieve this, we have fabricated open-faced graphene devices on an hBN substrate where the electrodes are used to both measure transport and selectively strain the graphene (Figure 1d,e). The graphene is aligned to the hBN using a gold-based transfer method that deterministically produces large moiré superlattices (see deterministic alignment of g-hBN samples in the Supporting Information).

Following our prior work on mechanically reconfigurable vdW devices,[25] we implement a moveable handle electrode that grips the graphene to slide and stretch it across the hBN. To selectively adhere the metal handle to the graphene only, we apply a light O_2-plasma treatment before depositing the Cr/Au handles. The treatment is sufficiently short that the graphene retains its structural integrity. The graphene-handle bond is strong enough to strain graphene beyond its tensile strength and tear it (Figure S4a,b). We found the plasma pretreatment to be critical, as thermally evaporated metals such as Au, Cr, and Ni exhibit low sliding friction on graphene and cannot overcome the friction of graphene aligned to hBN.

The devices are designed with a fixed source electrode and a moveable drain electrode that can be displaced laterally by pushing with an atomic force microscope (AFM) tip (Figure 1d,e), inducing heterostrain in the gripped graphene layer. The moveable electrode has sufficient sliding friction to retain the graphene strain when the AFM tip is retracted. The end result is an open-face graphene device that can be progressively strained independent of the hBN substrate. The graphene strain can be directly observed both in the physical displacement of the graphene edges (measured in AFM), as well as in Raman shifts of the graphene G peak, both showing that at least 0.6% strain can be fixed in the graphene layer (Figure S5a−d).

To image the effects of heterostrain on the g-hBN moiré, we performed conductive AFM (CAFM) on the open graphene channels (Figure 1f−h). An unstrained graphene is shown in Figure 1f, where the moiré pattern appears clearly in CAFM with a ∼14 nm wavelength, the maximum possible for unstrained g-hBN. By stretching the graphene via the gold handle, we observe a large elongation of the moiré along the strain direction, in line with the channel (Figure 1g,h). For the case in Figure 1h, the moiré lattice vector most aligned to the strain direction is stretched by 84% to 25.7 nm.

To analyze the stretched moiré structure, we extracted the moiré lattice vectors from the fast Fourier transform (FFT) of the CAFM images. We find that a uniaxial strain model can fit most device regions to within 1% of the extracted wavevectors. By assuming pure uniaxial graphene heterostrain, we can extract local values for the uniaxial strain (ε), strain direction (φ), relative graphene-hBN twist angle (θ), as well as the global orientation of the layers with respect to the AFM image (see Supporting Information Uniaxial Heterostrain Model and Fitting section).

To track the evolution of the moiré patterns under strain, we incrementally stretch our samples and perform CAFM imaging in a grid of locations to characterize the homogeneity. Figure 2a−d shows a sample of these for device B, as it is progressively stretched horizontally. We measure this sample in ten strained states and plot the measured moiré wavelengths versus the strain values extracted from our uniaxial strain model fits (Figure 2e). As the graphene is stretched, we observe that the moiré lattice vectors are elongated, depending on their orientation to the strain axis. The (purple) moiré vector, nearly aligned with the strain axis, is stretched up to 34% relative to 14 nm. This corresponds to a 0.46% uniaxial strain of the graphene aligned 5 ± 4° with respect to the AFM x-axis and the graphene channel. The (blue) moiré vector that is nearly perpendicular to the strain axis shows little change. The theoretical moiré wavelength for a 0° sample under uniaxial homostrain is plotted in green and shows a weak dependence on strain. It is clear then that by heterostraining our samples, we are able to achieve moiré wavelengths that would be impossible using homostrain.

We compare the moiré wavelength measurements to the expected values given by the average twist angle (θ = 0.022°) and uniaxial strain angle (φ = 18.279° with respect to the graphene lattice vector) extracted for all of the points (solid lines in Figure 2e). A majority of the data points are clustered

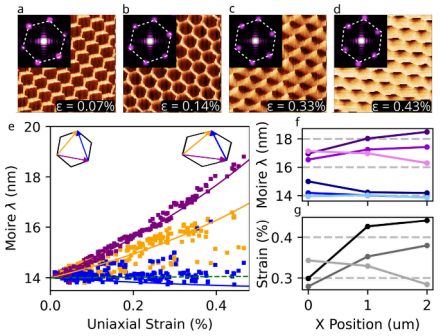

Figure 2. Progressive uniaxial strain and spatial uniformity in device B. All reported strain values have an average uncertainty of ±0.02% due to a 1% uncertainty in measuring the moiré wavevector. All parameters and uncertainties are listed in Supporting Information Table 1. (a−d) Sequence of 100 nm × 100 nm CAFM images of graphene-hBN moirés ordered from lower to higher strain (0.07% to 0.43%). Images are taken within ∼200 nm of the same location, and the x-axis is aligned along the graphene channel. Insets: FFT of the real space images. White hexagon overlay is the same for each panel as a reference to demonstrate the evolution of the lattice wavevectors with strain. (e) Plot of measured moiré wavelengths versus uniaxial graphene strain for 10 strained states. Lines are theoretical moiré wavelengths for a twist angle of 0.022° and strain angle of 18.279° with respect to the graphene lattice vector, that correspond to the average values for the data set. Insets illustrate the moiré unit cell orientation and stretch. (f) Moiré wavelength versus position for the most strained state. Blue/purple shaded points correspond to the blue/purple vectors in part e, respectively. Different hues correspond to different rows along the devices separated by vertical distances of 1 μm. The stretching electrode is located at an x position of 2.25 μm. (g) Graphene strain vs position (same strain state as f). Each line is a row along the device.

https://doi.org/10.1021/acs.nanolett.4c04201
Nano Lett. 2024, 24, 15662−15667

around the model lines, indicating the uniformity in the twist and strain angles in the sample. See Supporting Information Figure S8 for an example of a stretched device with a nonuniform twist angle.

The stretched moirés exhibits a consistent spatial variation across the channel, with the largest moiré wavelengths and strains near the stretching electrode. This effect is clearly seen in the final strained state in Figure 2f,g, where increasing x-position is closer to the stretching electrode on the right-side of the device. We attribute this strain gradient to the friction of the aligned g-hBN domains, as well as local pinning from sample edges and disorder, which prevents an ideal elastic response of the stretched graphene. Nonetheless, in the final state, the device is strained across its entire ∼2 μm length with a maximum wavelength that varies from 16.3 to 18.8 nm.

The large heterostrain with micrometer-scale uniformity achieved with our approach offers a unique opportunity to study the electronic properties of stretched moirés in transport. When graphene is aligned to hBN, superlattice-induced band gaps emerge at the edge of the reduced moiré Brillouin zone (Figure 3a). In transport measurements, this results in new superlattice resistance peaks at densities of $n = \pm 4/$(moiré unit cell area), where the peak at hole doping is more prominent (Figure 3b). As the aligned graphene is stretched, we observe the superlattice resistance peak to progressively shift closer to the primary Dirac peak at charge neutrality. Compressing the channel shifts the peak in the opposite direction. This effect is consistent with heterostrain causing a substantial modification of the moiré unit cell area. At the maximum strained state, the superlattice peak has moved 29% closer to the main Dirac peak, suggesting a corresponding increase in the moiré unit cell area.

To further analyze the behavior of the superlattice resistance peak, we compare moiré areas extracted from the resistance peak position to moiré areas measured by CAFM. We plot these in Figure 3c for multiple devices in different strained states. Due to the applied heterostrain, many of the data points exceed the maximum area for unstrained, aligned g-hBN of $\sqrt{(3)}/2\ (14\ \text{nm})^2 \sim 170\ \text{nm}^2$ (black diamond). The horizontal spread in CAFM areas is due to strain and twist angle inhomogeneity within each device. For small moirés, there is agreement between the areas extracted from transport and CAFM. However, for stretched moirés beyond ∼14 nm, the moiré area extracted from transport consistently exceeds the area measured in CAFM. We ascribe this effect to the reduced electronic bandwidths of the stretched g-hBN devices. Similar effects have been observed in room temperature measurements of twisted bilayer graphene.[18,26] Indeed, cooling devices B and C to 1.6 K removes the discrepancy between the transport and CAFM areas (see the Supporting Information Superlattice Dirac Peak Temperature Dependence section).

At cryogenic temperatures, applying a perpendicular magnetic field to devices with nearly uniform heterostrain results in Landau fans emerging from the charge neutrality point and the hole-side superlattice peak (Figure 3d and Figure S11). Figure 3d shows magnetotransport data for device C, which has an average uniaxial strain of 0.30 ± 0.04%, twist angle of 0.03 ± 0.04°, and strain angle of 9 ± 4° with respect to the graphene lattice vector, where the uncertainties are the standard deviation of the values measured at different sample positions. Fan features emerge from a sharp superlattice peak corresponding to a moiré area of 221 ± 3 nm^2, which is close to the average areas measured by CAFM at room temperature

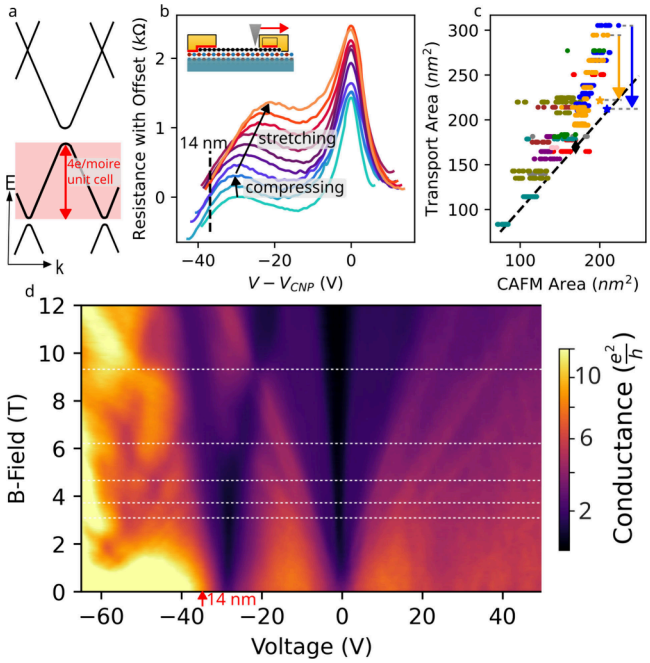

Figure 3. Effects of uniaxial heterostrain on the transport properties of graphene-hBN devices. (a) Cartoon band structure of aligned g-hBN at zero strain. Each moiré subband corresponds to 4 electrons per moiré unit cell area. (b) Room temperature gate sweeps of device B show the superlattice peak shifting due to AFM manipulation. Sequential traces are offset for clarity. The measurements are made *in situ* to the AFM immediately after manipulating. The first two manipulations are compressive, and the last seven are stretching motions. The dashed black line indicates the expected location of the superlattice peak for the largest unstrained moiré, corresponding to a 14 nm wavelength. Note that the device as-fabricated has a built-in strain that varies from 0.01% to 0.13%. Inset: device manipulation schematic. (c) Moiré unit cell area measured from CAFM images versus the area extracted from the superlattice resistance peak position via transport. Marker colors differentiated 10 devices. Circle markers correspond to transport data taken under ambient conditions. The two star markers correspond to transport data taken at 1.6 K (plotted at the average CAFM area). Devices B and C are colored blue and orange, respectively. The black dashed line denotes equal CAFM and transport areas. (d) Magnetoconductance data of device C taken at 1.6 K. Horizontal white lines overlaid correspond to a magnetic flux of 1/2, 1/3, 1/4, 1/5, 1/6 flux quanta per moiré unit cell area (221 ± 3 nm^2). A contact resistance value of 4.43 kΩ is subtracted to align the $\nu = 2$ plateau to 2 e^2/h.

(200 ± 10 nm^2). Due to the stretched moiré unit cell size, the primary Landau fan is disrupted at lower magnetic fields than is typical for g-hBN devices.[27,28] These disruptions arise due to the collisions of the primary and superlattice Landau fans, with intersections occurring at B field values of 1 flux quanta per integer number of moiré unit cells, $B = \varphi_0/(q \cdot A_m)$, where B is the magnetic field, φ_0 is the magnetic flux quanta, A_m is the moiré unit cell area, and q is an integer (horizontal lines in Figure 3d). We conclude that the heterostrain is sufficiently uniform to produce coherent superlattice modulation of the transport features consistent with a stretched moiré unit cell.

Another characteristic of aligned g-hBN devices is the presence of an insulating state at charge neutrality due to the breaking of graphene inversion symmetry by the aligned hBN.[28,29] In the heterostrained devices, we only observe a weak insulating-like dependence at the charge neutrality point or at the superlattice point for our heterostrained devices. We

https://doi.org/10.1021/acs.nanolett.4c04201
Nano Lett. 2024, 24, 15662−15667

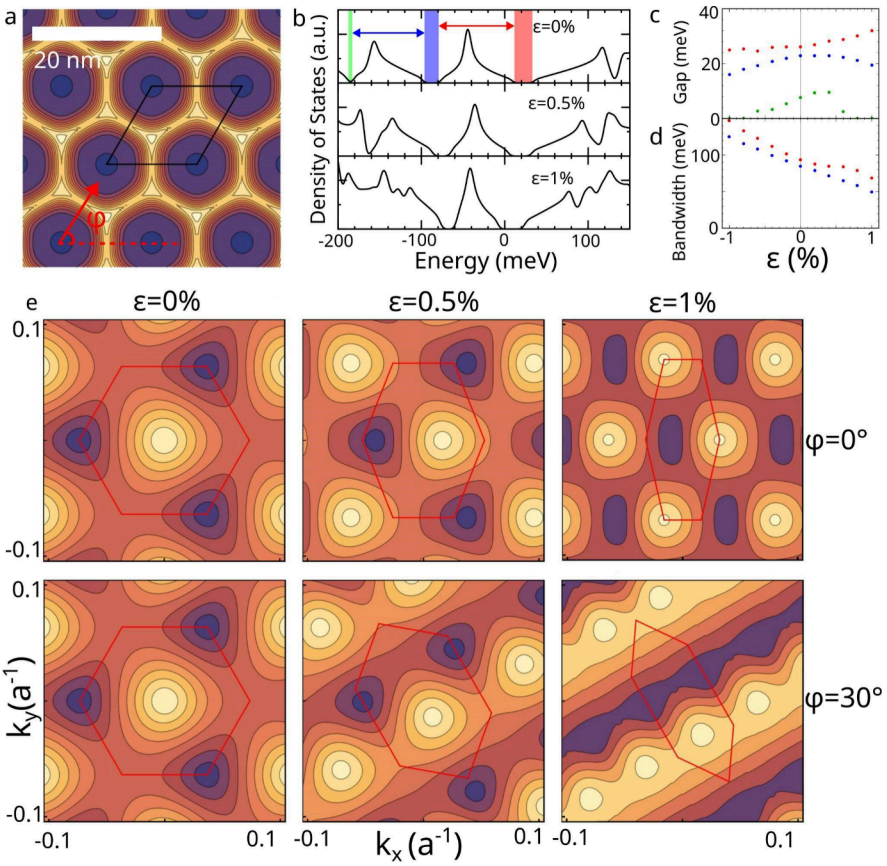

Figure 4. Electronic structure of heterostrained graphene aligned to hBN with 0° twist angle. (a) Real space plots show the local binding energy between the graphene and hBN lattices. Contour intervals are 0.2 eV/nm^2. The moiré unit cell and strain angle with respect to the graphene lattice vectors are illustrated. (b) Density of states plots for ε = 0%, 0.5%, and 1% at φ = 0°. Highlighted regions and arrows indicate gaps and bandwidths for parts c and d. (c) Primary, secondary, and tertiary gap sizes versus strain at φ = 0. (d) First and second hole miniband bandwidth versus strain at φ = 0. (e) Band structure contour plots of the first hole miniband for ε = 0%, 0.5%, and 1% at φ = 0° and φ = 30°. Wavevector units are expressed in terms of the graphene lattice constant, *a*. Red hexagons show the moiré Brillouin zones. Contour intervals are 10 meV.

ascribe this to strain and charge inhomogeneity in the device, where the latter is known to play an important role in obscuring insulating states in graphene devices due to edge doping effects.[30,31]

To analyze the effects of heterostrain on the electronic structure of the g-hBN moiré, we theoretically calculate the band structure using a continuum model that includes lattice relaxation (Figure 4, details in the Supporting Information theory section). The simplest effect of the uniaxial heterostrain is to shrink the moiré Brillouin zone (BZ), reducing the carrier density per superlattice miniband. This results in a reduced bandwidth of the first hole miniband, which shrinks by 41.9% for 1% uniaxial strain applied along the graphene lattice vector (zero strain angle). Under the same strain conditions, the primary Dirac point gap grows by 22.7% and the first hole superlattice gap decreases by 15.5%. Straining along different directions causes different changes to the gap sizes, but the primary and hole superlattice gaps remain open up to 1% strain, independent of the strain angle.

These basic theoretical results are in line with our experimental observations of the shifting of the superlattice resistance peak as strain increases the size of the moiré unit cell. Because both the primary and hole-side superlattice gaps remain open as the graphene is stretched, the carrier density of the hole miniband remains at 4 electrons per superlattice unit cell, which is consistent with the match between our cryogenic transport measurements of the superlattice hole peak and the CAFM-extracted moiré area. By contrast, the electron-side superlattice band edge remains gapless with applied strain, consistent with our lack of observation of an electron-side superlattice resistance peak. Moreover, the decrease in bandwidth with uniaxial strain is consistent with the discrepancy with the moiré area extracted from room temperature measurements as compared with CAFM and cryogenic measurements. At room temperature, thermal energy is a significant fraction of the bandwidth of the first hole miniband, with increased thermal excitation expected as the bandwidth is reduced with 1% heterostrain from 85 to 49 meV for zero strain angle (Figure 4).

Heterostrain introduces strong anisotropy in the graphene electronic structure, where the Fermi surface near the hole superlattice gap becomes stretched and can even become quasi-one-dimensional due to the heterostrain. For zero strain angle, the anisotropy is apparent in the effective mass at the bottom of the hole miniband, where m_y/m_x = 3.63, corresponding to the ratio of the effective mass in the direction of the strain versus perpendicular for 1% uniaxial strain and zero strain angle. This is contrasted with the Fermi surfaces around the primary Dirac point, which are less sensitive to the distorted moiré and remain effectively isotropic under the effects of the 1% graphene strain. For the 30° strain angle, open Fermi surfaces dominate the electronic band

https://doi.org/10.1021/acs.nanolett.4c04201
Nano Lett. 2024, 24, 15662−15667

structure for large heterostrain (Figure 4e). These open Fermi surfaces are strongly anisotropic and quasi-one-dimensional, where the Fermi velocity is limited to a range of directions along a preferred propagation direction.

In summary, we present a method to controllably introduce a large heterostrain in a g-hBN device. The induced heterostrain is sufficiently homogeneous to observe a modified electronic structure corresponding to the stretched moiré pattern. These overall observations are in agreement with the reduced bandwidth and BZ size observed in theoretical calculations, which also predict that heterostrain should introduce anisotropy into the effective masses and open Fermi surfaces. In future studies, multiterminal devices with different strain angles will be able to probe the effects of the anisotropic electronic structure. We note that even larger strain values are achievable locally using this technique, where we have observed local moiré patterns ∼70 nm long correspond to ∼1.4% level strains (see Supporting Information Figure S9).

For this work, we used an AFM tip to set the strain in our devices, but we envision that other actuation methods, such as bending, piezoelectric actuation, or thermal contraction, can be used to achieve *in situ* manipulation, even at cryogenic temperatures. Moreover, our methods should apply to other types of crystals supported on hBN, especially twisted graphene and transition metal dichalcogenide multilayers, where strain control can be used to deterministically break the symmetry of moiré patterns, manipulate the structure of pseudomagnetic fields and electronic flatbands, or alternatively be used as a method to reduce strain in a device unintentionally introduced by nanofabrication.

■ ASSOCIATED CONTENT

Supporting Information

The Supporting Information is available free of charge at https://pubs.acs.org/doi/10.1021/acs.nanolett.4c04201.

Additional experimental details, materials, methods, and theoretical model (PDF)

■ AUTHOR INFORMATION

Corresponding Author

Javier D. Sanchez-Yamagishi − *Department of Physics and Astronomy, University of California, Irvine, Irvine, California 92697, United States;* orcid.org/0000-0001-9703-6525; Email: javier.sanchezyamagishi@uci.edu

Authors

Ian Sequeira − *Department of Physics and Astronomy, University of California, Irvine, Irvine, California 92697, United States*

Andrew Z. Barabas − *Department of Physics and Astronomy, University of California, Irvine, Irvine, California 92697, United States*

Aaron H Barajas-Aguilar − *Department of Physics and Astronomy, University of California, Irvine, Irvine, California 92697, United States*

Michaela G Bacani − *Department of Physics and Astronomy, University of California, Irvine, Irvine, California 92697, United States*

Naoto Nakatsuji − *Department of Physics, Osaka University, Toyonaka, Osaka 560-0043, Japan*

Mikito Koshino − *Department of Physics, Osaka University, Toyonaka, Osaka 560-0043, Japan*

Takashi Taniguichi − *Research Center for Materials Nanoarchitectonics, National Institute for Materials Science, Tsukuba 305-0044, Japan;* orcid.org/0000-0002-1467-3105

Kenji Watanabe − *Research Center for Electronic and Optical Materials, National Institute for Materials Science, Tsukuba 305-0044, Japan;* orcid.org/0000-0003-3701-8119

Complete contact information is available at: https://pubs.acs.org/10.1021/acs.nanolett.4c04201

Author Contributions

†I.S. and A.Z.B. contributed equally to this work.

Notes

The authors declare no competing financial interest.

■ ACKNOWLEDGMENTS

We acknowledge the use of facilities and instrumentation at the Integrated Nanosystems Research Facility (INRF), in the Samueli School of Engineering at the University of California Irvine, and at the UC Irvine Materials Research Institute (IMRI), which is supported in part by the National Science Foundation through the UC Irvine Materials Research Science and Engineering Center (Grant DMR-2011967). We thank L. Jauregui, S. Nam, D. Goldhaber-Gordon, and A. F. Young for productive discussions, as well as the technical assistance of Q. Lin, R. Chang, M. Kebali, and J. Hes. We also thank D. Velarde, F. A. Bonilla, and S. Kaemmer at Park Systems for their suggestions and technical assistance. This work was partially supported by the National Science Foundation Materials Research Science and Engineering Center program through the UC Irvine Center for Complex and Active Materials Grant DMR-2011967 and the National Science Foundation Career Award DMR-2046849. I.S. acknowledges fellowship support from the UCI Eddleman Quantum Institute. K.W. and T.T. acknowledge support from the JSPS KAKENHI (Grants 21H05233 and 23H02052) and World Premier International Research Center Initiative (WPI), MEXT, Japan. N.N and M.K. acknowledge support from the JSPS KAKENHI (Grants JP21H05236 and JP21H05232) and by JST CREST (Grant JPMJCR20T3), Japan.

■ REFERENCES

(1) Inbar, A.; et al. The quantum twisting microscope. *Nature* **2023**, *614*, 682−687.
(2) Ribeiro-Palau, R.; et al. Twistable electronics with dynamically rotatable heterostructures. *Science* **2018**, *361*, 690−693.
(3) Yang, Y.; et al. In situ manipulation of van der Waals heterostructures for twistronics. *Sci. Adv.* **2020**, *6*, No. eabd3655.
(4) Kapfer, M.; et al. Programming twist angle and strain profiles in 2D materials. *Science* **2023**, *381*, 677−681.
(5) Alden, J. S.; et al. Strain solitons and topological defects in bilayer graphene. *Proc. Natl. Acad. Sci. U. S. A.* **2013**, *110*, 11256−11260.
(6) Kögl, M.; et al. Moiré straintronics: a universal platform for reconfigurable quantum materials. *npj 2D Mater. Appl.* **2023**, *7*, 32.
(7) Escudero, F.; Sinner, A.; Zhan, Z.; Pantaleón, P. A.; Guinea, F. Designing moiré patterns by strain. *Phys. Rev. Res.* **2024**, *6*, No. 023203.
(8) Finney, J.; et al. Unusual magnetotransport in twisted bilayer graphene. *Proc. Natl. Acad. Sci. U. S. A.* **2022**, *119*, No. e2118482119.
(9) Wang, X.; et al. Unusual magnetotransport in twisted bilayer graphene from strain-induced open Fermi surfaces. *Proc. Natl. Acad. Sci. U. S. A.* **2023**, *120*, No. e2307151120.

(10) Bi, Z.; Yuan, N. F. Q.; Fu, L. Designing flat bands by strain. *Phys. Rev. B* **2019**, *100*, No. 035448.
(11) Kerelsky, A.; et al. Maximized electron interactions at the magic angle in twisted bilayer graphene. *Nature* **2019**, *572*, 95−100.
(12) Huder, L.; et al. Electronic Spectrum of Twisted Graphene Layers under Heterostrain. *Phys. Rev. Lett.* **2018**, *120*, No. 156405.
(13) Mesple, F.; et al. Heterostrain Determines Flat Bands in Magic-Angle Twisted Graphene Layers. *Phys. Rev. Lett.* **2021**, *127*, No. 126405.
(14) Qiao, J.-B.; Yin, L.-J.; He, L. Twisted graphene bilayer around the first magic angle engineered by heterostrain. *Phys. Rev. B* **2018**, *98*, No. 235402.
(15) Xie, Y.; et al. Spectroscopic signatures of many-body correlations in magic-angle twisted bilayer graphene. *Nature* **2019**, *572*, 101−105.
(16) Choi, Y.; et al. Electronic correlations in twisted bilayer graphene near the magic angle. *Nat. Phys.* **2019**, *15*, 1174−1180.
(17) Bai, Y.; et al. Excitons in strain-induced one-dimensional moiré potentials at transition metal dichalcogenide heterojunctions. *Nat. Mater.* **2020**, *19*, 1068−1073.
(18) Zhang, L.; et al. Correlated States in Strained Twisted Bilayer Graphenes Away from the Magic Angle. *Nano Lett.* **2022**, *22*, 3204−3211.
(19) Gao, X.; et al. Heterostrain-enabled dynamically tunable moiré superlattice in twisted bilayer graphene. *Sci. Rep.* **2021**, *11*, 21402.
(20) Wang, L.; et al. In Situ Strain Tuning in hBN-Encapsulated Graphene Electronic Devices. *Nano Lett.* **2019**, *19*, 4097−4102.
(21) Liu, Z.; et al. Continuously tunable uniaxial strain control of van der Waals heterostructure devices. *J. Appl. Phys.* **2024**, *135*, No. 204306.
(22) Peña, T.; et al. Strain engineering 2D MoS_2 with thin film stress capping layers. *2D Mater.* **2021**, *8*, No. 045001.
(23) Zhang, Y.; Zhao, H. L.; Huang, S.; Hossain, M. A.; Van Der Zande, A. M. Enhancing Carrier Mobility in Monolayer MoS_2 Transistors with Process-Induced Strain. *ACS Nano* **2024**, *18*, 12377−12385.
(24) Zhang, Y.; et al. Patternable Process-Induced Strain in 2D Monolayers and Heterobilayers. *ACS Nano* **2024**, *18*, 4205−4215.
(25) Barabas, A. Z.; et al. Mechanically reconfigurable van der Waals devices via low-friction gold sliding. *Sci. Adv.* **2023**, *9*, No. eadf9558.
(26) Polshyn, H.; et al. Large linear-in-temperature resistivity in twisted bilayer graphene. *Nat. Phys.* **2019**, *15*, 1011−1016.
(27) Ponomarenko, L. A.; et al. Cloning of Dirac fermions in graphene superlattices. *Nature* **2013**, *497*, 594−597.
(28) Hunt, B.; et al. Massive Dirac Fermions and Hofstadter Butterfly in a van der Waals Heterostructure. *Science* **2013**, *340*, 1427−1430.
(29) Jung, J.; DaSilva, A. M.; MacDonald, A. H.; Adam, S. Origin of band gaps in graphene on hexagonal boron nitride. *Nat. Commun.* **2015**, *6*, 6308.
(30) Aharon-Steinberg, A.; et al. Long-range nontopological edge currents in charge-neutral graphene. *Nature* **2021**, *593*, 528−534.
(31) Cui, Y.-T.; et al. Unconventional Correlation between Quantum Hall Transport Quantization and Bulk State Filling in Gated Graphene Devices. *Phys. Rev. Lett.* **2016**, *117*, No. 186601.

https://doi.org/10.1021/acs.nanolett.4c04201
Nano Lett. 2024, 24, 15662−15667